

High-Resolution *Ex Vivo* Elastography to Characterize Tumor Stromal Heterogeneity *In Situ* in Pancreatic Adenocarcinoma

Phuong Vincent , Hexuan Wang, Michael Nieskoski, Jason R. Gunn, Kalya Marra, P. Jack Hoopes, Kimberley S. Samkoe, Marvin M. Doyley , Tayyaba Hasan , and Brian W. Pogue 

I. INTRODUCTION

Abstract—Objective: Tumor stiffening in pancreatic adenocarcinoma (PDAC) has been linked to cancer progression and lack of therapy response, yet current elastography tools cannot map stiffness in a whole tumor field-of-view with biologically relevant spatial resolution. Therefore, this study was developed to assess stiffness heterogeneity and geometrical patterns across whole PDAC xenograft *ex vivo* tumors. **Methods:** The *ex vivo* elastography (EVE) mapping system was capable of creating stiffness map at 300-micron spatial resolution under a 5–20 mm field of view relevant to whole tumor assessment. The stiffness value at each location was determined by compression testing and an absolute tumor Young's modulus map was calculated based on the calibration between the system and ultrasound elastography ($R^2 = 0.95$). **Results:** Two PDAC tumor lines AsPC-1 and BxPC-3 implanted in xenograft models were assessed to show tumor stiffness and its linear relationship to collagen content ($R^2 = 0.59$). EVE was able to capture stiffness heterogeneity ranging between 5 and 100 kPa in pancreatic tumors with collagen content up to 25%. More importantly, data shows the inverse relationship of local stiffness to local drug distribution ($R^2 = 0.66$) and vessel patency ($R^2 = 0.61$) in both PDAC tumor lines. **Conclusion:** The results suggested that elastography could be utilized to predict drug penetration in PDAC tumors or assess response to biological modifying adjunct therapies. **Significance:** This study presents the first attempt to map out stiffness on a biologically relevant spatial scale across whole PDAC tumor slices with spatial resolution in the hundreds of microns.

Index Terms—Elastography, Histopathology image color analysis, Optical Interferometry, Fabry-Perot, Pancreatic Tumor Microenvironment Heterogeneity.

POOR vascular perfusion leading to low drug penetration persists as a major problem in solid tumor cancer therapeutics [1] and is especially prominent in pancreatic adenocarcinoma (PDAC). When surgical resection is limited by tumor invasion into surrounding major blood vessels, almost all therapeutic options rely upon delivering systemic pharmacologic drugs into the tumor. Understanding and improving tumor drug transport efficiency therefore will benefit chemotherapy, immunotherapy and combinations of any targeted therapies [2] in this aggressive disease. The inherent drug-resistant nature of PDAC stems from two well-studied phenomena: the heterogeneity of genetic mutations and desmoplastic tumor microenvironment [3]. Therapies targeting cancer-associated genetic pathways yield mixed results [4]–[6] since the complexity of molecular signaling mechanisms could lead to upregulation of compensatory pathways. Meanwhile, the dense stroma characteristic of PDAC results in elevated total tissue pressure [7] that damages tumor vasculature [8] and the lymphatic system [9]. Active research on the multifaceted origin of poor tumor transport has not only improved our understanding on the underlying biological mechanisms but has also emphasized the clinical need for a biomarker that could reflect drug transport efficiency, and the resulting therapeutic response. The daunting search for such a biomarker faces an intrinsic dilemma of spatial size scale mismatch: the micron-scale associated with meaningful genetic and/or biological tumor information versus the clinical need to acquire this data on the centimeter-scale relevant to whole tumor size.

Fortunately, recent findings from both ends of the aforementioned spatial scale range have reported that tumor stiffness could be a potential tool to address drug transport and therapy response. Laklai *et al.* (2010) provided the first direct evidence that linked tumor genotype with desmoplasia, the two constraints of PDAC drug-resistant nature [10]. In this study, tumor stiffness was obtained by atomic force microscopy and data from both clinical and preclinical samples confirmed the potential of elastography to reflect tumor biology changes related to cancer progression and aggression. On the mesoscopic scale, Harada *et al.* (2017) echoed the linear relationship between tissue stiffness and fibrosis content by showing ultrasound elastography and pathology data from a single patient [11].

Manuscript received July 22, 2019; revised November 11, 2019; accepted December 28, 2019. Date of publication January 1, 2020; date of current version August 20, 2020. This work was funded by NIH grant P01 CA084203. (Corresponding author: Brian W. Pogue.)

P. Vincent, M. Nieskoski, J. R. Gunn, and K. Marra are with the Thayer School of Engineering, Dartmouth College.

H. Wang and M. M. Doyley are with the Department of Electrical and Computer Engineering, University of Rochester.

P. J. Hoopes and K. S. Samkoe are with the Thayer School of Engineering, Dartmouth College, and also with the Department of Surgery, Geisel School of Medicine, Dartmouth College.

T. Hasan is with the Wellman Center for Photomedicine, Massachusetts General Hospital, Harvard Medical School.

B. W. Pogue is with the Thayer School of Engineering, Dartmouth College, Hanover, NH 03755 USA (e-mail: brian.w.pogue@dartmouth.edu).

Digital Object Identifier 10.1109/TBME.2019.2963562

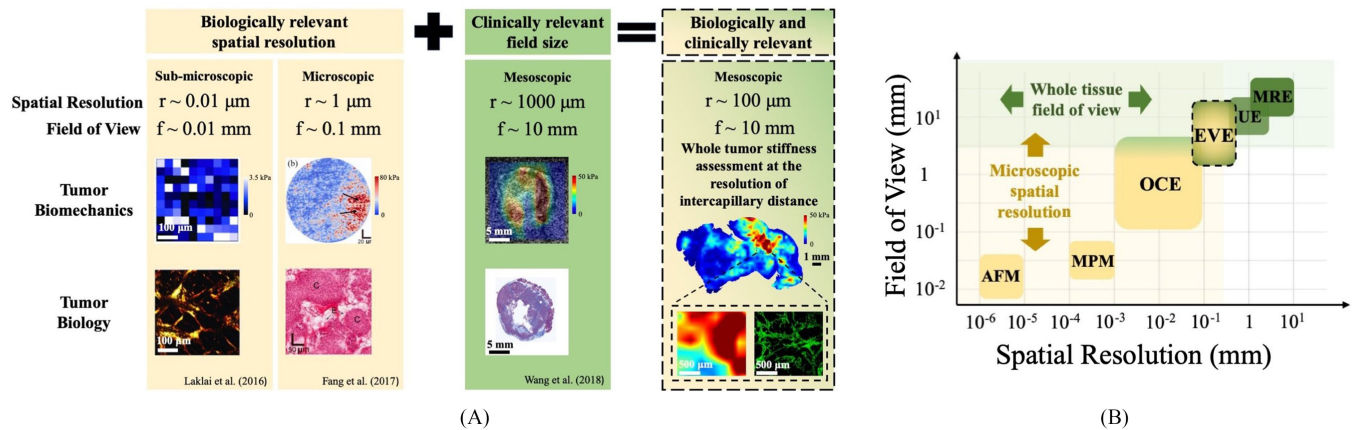


Fig. 1. Current experimental techniques for assessing features related to tumor stiffness. **(A)** Tumor biomechanics and relevant biology information are actively studied at different spatial scales: sub-microscopic [10], microscopic [12] and mesoscopic [13]. Current elastography tools offer either biologically relevant spatial resolution or clinically relevant field of view, none exists that could meet both requirements. Stiffness information as a clinical application to evaluate drug transport brings most benefit when whole tumor stiffness is assessed at inter-capillary distance spatial resolution. **(B)** Common elastography assessment tools and their positions in the field include AFM: atomic force microscopy, MPM: multi-photon microscopy harmonic imaging, OCE: optical coherence elastography, UE: ultrasound elastography, MRE: magnetic resonance elastography. Ideal elastography imaging tools should be placed in the overlap between microscopic resolution region and whole-tissue FOV region. Since no current imaging tool could meet these requirements, ex vivo elastography (EVE) mapping was developed to study PDAC stiffness at relevant biological size scales, with 300- μm spatial resolution and a field of view that would cover a whole PDAC tumor.

Ultrasound elastography was also used by Wang *et al.* (2018) to obtain wide-field stiffness information, which was linearly correlated with tumor collagen but inversely correlated with PDAC tumor drug distribution [14]. While these findings underscore the potential use of stiffness imaging, current experimental elastography tools [15] do not meet the two requirements of having biologically meaningful spatial resolution and a clinically relevant field of view. **Fig. 1B** illustrates basic elastography tools with atomic force microscopy (AFM) and multiphoton microscopy harmonic imaging (MPM) being widely explored to characterize very small regions of tissue. Optical coherence elastography (OCE) or ultrasound elastography (UE) are non-invasive, however OCE has a small field of view ($f < 1 \text{ mm}$, up to 5 mm with a translation stage) with high spatial resolution ($r \approx 0.01 \text{ mm}$) while UE has a higher field of view ($f \approx 10 \text{ mm}$) but limited spatial resolution ($r \approx 1 \text{ mm}$).

In order to study PDAC tumor stiffness at a clinically relevant size scale with biologically meaningful spatial resolution, we developed a novel, cost-effective ex vivo elastography (EVE) mapping system. EVE equipped by a translation stage was able to map tumor stiffness at 300-micron resolution in pancreatic xenograft tumors with 1-cm diameter. This spatial resolution is sufficient to study tumor drug distribution, since intratumoral transport primarily relies on diffusion between blood vessels [1]. Additionally, our previous studies have showed that the spatial scale of relevant variation in tumor solid stress is hundreds of microns, matching the known intercapillary distances [16]. Stiffness of the tumor also appears to be linked to the complexity [16] and thickness [10] of the collagen grown within the desmoplastic tissue. Therefore, EVE provides an adequate spatial resolution and field of view so that elastography information could be assessed globally and regionally, compensating for both microscopic and mesoscopic elastography tools (**Fig. 1A**). In this study, the methodology for whole-tumor stiffness mapping was

developed and verified with data from two orthotopic PDAC xenograft models. The relationship between stiffness and tumor microenvironment was examined by quantifying tumor collagen from pathology images to provide direct visualization of stiffness and stroma variations in whole-tumor size. Finally, tumor transport parameters such as patent vessels and drug distribution via fluorescence imaging were investigated to determine the spatial relationship between stiffness, perfused vasculature and resulting drug penetration.

II. METHODS

A. Ex Vivo Elastography (EVE) Mapping System

The system consisted of a fiber optic pressure sensor FOP-M260 (FISO, Quebec, Canada) coupled with a three-dimensional motorized translation table (Velmex, Bloomfield, NY) illustrated in **Fig. 2A**. The x-y dimension (table part# MAXY4009, stepping motor part# PK266-03A) was responsible for tracking the spatial coordinates across the tumor surface, and the z-dimension (table part# MA4006, stepping motor part# PK266-03B) controlled the compression displacements applied to determine strain and corresponding pressure values. The pressure sensor operates based on Fabry-Perot interferometer technology (**Fig. 2C**). This pressure sensor has been utilized in both preclinical and clinical settings [17]–[19]. In this application, the pressure readings were converted into electrical signals in the range of 0-5V using the FISO signal conditioning module (part# FPI-LS, FISO, Quebec, Canada). The analog was input to LabVIEW via a data acquisition device USB-6008 (National Instruments, Austin, TX). Pressure data had a resolution of 0.02 kPa and accuracy of 0.13 kPa. The pressure detection range is $\pm 40 \text{ kPa}$ relative to atmospheric pressure. The pressure sensor and the motorized xyz table were controlled by LabVIEW and a simplified flowchart on data acquisition is illustrated in **Fig. 2E**.

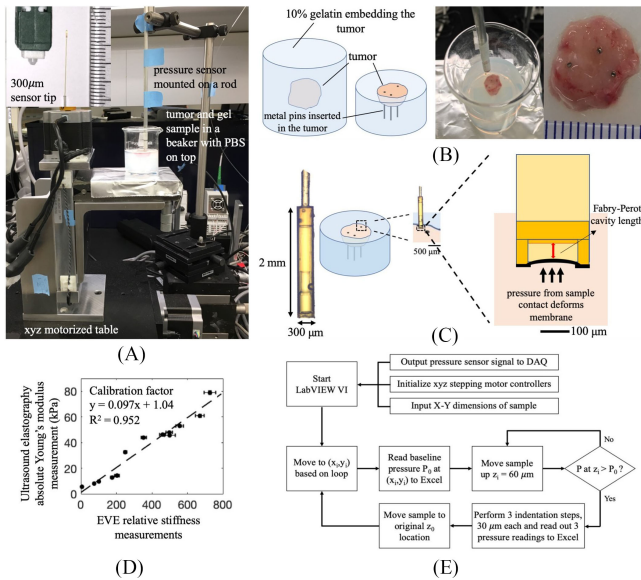


Fig. 2. *Ex vivo* elastography (EVE) system and sample preparation. (A) Overall system consists of an xyz- motorized table and a commercial fiber optic pressure sensor. (B) Sample preparation procedure includes a tumor embedded in 10% gelatin. Metal pins are inserted to provide markers for image coregistration with pathology data. (C) Pressure sensor operates based on Fabry-Perot interferometer technology. The cavity deformation due to external force is calibrated to give a corresponding pressure reading. (D) Young's modulus calibration curve between UE and EVE established by phantom measurements at different concentrations and temperatures. (E) A simplified flow chart illustrates important steps of stiffness measurement, which includes tumor surface identification and 3-step compression testing.

Mapping grid size was adjustable based on the tumor size. On an average tumor surface of 10×10 mm, imaging with the $300\text{-}\mu\text{m}$ resolution probe resulted in a grid size of 35×35 points.

EVE validation testing was carried out with agar phantoms to ensure the system could detect relative changes in pressure readings under tumor tissue measuring condition illustrated in Fig. 2A. Given that the mouse tumor sample thickness was on average 5 mm (L_0), $100\text{-}\mu\text{m}$ total deformation yielded a maximum of 2% strain ensuring tissue linear elasticity. At least three pressure measurements were required to generate a stress-strain curve whose slope was used to determine stiffness, therefore, three indentations (ΔL) were selected to be 30, 60 and $90\text{ }\mu\text{m}$. At each location, relative stiffness readings were calculated by measuring the slope of the stress-strain curve. For each of 6 varying concentrations of agar phantoms (1%, 1.2%, 1.5%, 1.6%, 1.8% and 2% agar), 21 relative stiffness measurements from 3 samples were obtained. Results from this test showed that EVE was able to detect the linear relationship between increasing agar concentration phantoms and increasing stiffness ($R^2 = 0.98$). There was no significant difference in phantom measurements obtained with and without the beaker confinement illustrated in Fig. 2(A)–(B). More importantly, stiffness readings obtained from a flat phantom surface (27 ± 3.0 kPa) and from a 15° inclined surface (27 ± 2.4 kPa) were consistent. This test provided evidence that EVE is sufficient to measure stiffness from samples with a high surface irregularity,

an inherent characteristic of fresh tissue with high stiffness such as solid pancreatic tumors. Tumor surface detection thus was extended and largely contributed to the average imaging time of 2 hours per tumor.

To convert from relative stiffness measurements to absolute Young's modulus values, EVE system was calibrated by a UE system. The UE system consisted of a Vantage 64 Ultrasound Scanner (Verasonics Inc.) and an L7-4 (Phillips Healthcare) linear transducer array. UE data was collected by using a $400\text{-}\mu\text{s}$, 7-kHz push pulse to induce shear waves. Young's modulus calculation for this system is described in Wang *et al.* under "Modulus estimation" [13]. A series of gelatin phantoms was fabricated to determine the calibration factor between the EVE relative stiffness measurements and absolute Young's modulus in kPa generated by UE. The calibration curve between two systems is illustrated in Fig. 2D. The feasibility of EVE system to produce correct stiffness maps is verified by measurement data from murine organs such as pancreas and spleen tissue. Validation results from this experiment are further discussed in Section IIIA.

B. Animal and Tumor Model

All animal procedures were conducted under the protocol approved by the Dartmouth Institutional Animal Care and Use Committee (IACUC). 27 athymic nude mice between the age of 6–8 weeks were used in this study. 13 mice were injected with human tumor cell line AsPC-1 (ATCC, Cat# CRL-1682) and the other 14 with BxPC-3 (ATCC, Cat# CRL-1687). The pancreas was exposed and tumor cells were injected with a 1:1 ratio of Matrigel. AsPC-1 and BxPC-3 required 2–4 weeks and 5–7 weeks, respectively, for tumors to reach ideal imaging size of 1 cm in diameter. The mice were on purified diet to reduce autofluorescence from food consumption.

C. Tumor Sample Preparation

After the tumors reached imaging size, the mice were anesthetized and sacrificed. The resected tumor was then embedded in gel. The gel block consisted of 10% gelatin, 1% cornstarch and 89% water designed to be just stiff enough to hold the bulk of the tumor. The gelatin phantom was sliced in half to provide a flat imaging surface for stiffness mapping (Fig. 2B). Three metal pins were inserted into the tumor to provide fiducial markers [20] for image co-registration between the stiffness map and pathology data. A layer of PBS was applied on the tumor surface to maintain proper hydration. Stiffness measurements from both gelatin and tumor samples confirmed no dehydration problem existed.

D. Drug Uptake Quantification via Fluorescence Imaging

Verteporfin or BPD (USP, Rockville, MD, USA) was dissolved in dimethyl sulfoxide at 1 mg/ml then diluted with PBS to obtain a final concentration of 0.1 mg/ml. Lectin (Vector Laboratories, Cat#FL-1211) at a concentration of 2 mg/ml was used as vascular patency marker. BPD (1 mg/kg) and lectin

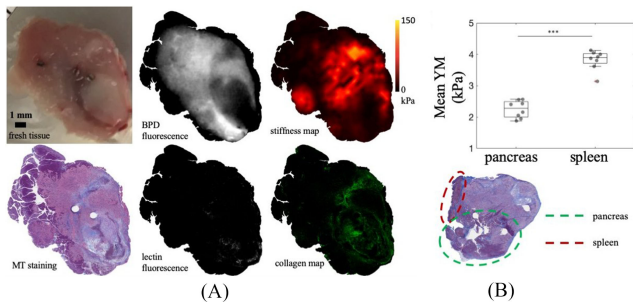


Fig. 3. Image data and tissue parameter identification process. (A) Top row from left to right: fresh tumor surface in gel with inserted metal pins, BPD fluorescence, stiffness map. Bottom row: Masson's Trichrome staining, lectin fluorescence, segmented collagen map from MT staining. All images are co-registered to MT staining data. (B) Average stiffness detected from spleen (4.0 ± 0.3 kPa) and pancreas (2.3 ± 0.3 kPa). These regions are excluded from tumor analysis by manual ROI drawn on pathology data.

(2 mg/kg) were injected intravenously one-hour and 2-minutes, respectively, before sacrifice. Seven out of 13 AsPC-1 mice and 7 out of 14 BxPC-3 mice received these injections. After slicing the gel to expose the tumor surface, fluorescence imaging was immediately performed on fresh tissue by a flatbed scanner (GE Typhoon 700) using a 473 nm excitation source with a 670 nm LP filter. Vascular patency was determined by fluorescence imaging of lectin using a PerkinElmer Vectra3 slide scanner with a FITC filter.

E. Tumor Biological Parameter Identification

After stiffness mapping, the tumors were fixed in 10% formalin and sectioned at 4-micron thickness. H&E staining was used to identify tumor tissue while Masson's Trichrome (MT) identified collagen fibers by blue staining. All image data was co-registered to MT image (Fig. 3A) using a rigid transformation in MATLAB. The blue collagen map was segmented from the MT image by converting from RGB to HSV color space and thresholding for blue pixels ($0.5 < \text{hue} < 0.7$, saturation > 0.5 for BxPC-3 and saturation > 0.3 for AsPC-1, value > 0.7). A different saturation cutoff for each tumor line was necessary to make sure segmented maps truly reflect collagen content within the tumors. Collagen percentage was obtained by finding the ratio of blue pixels over the total tumor tissue area. H&E image was used to identify and exclude non-tumor tissue from analysis. Fig. 3B showed an example of a tumor sample with pancreas and spleen tissue attached. ROIs for these regions were manually drawn and subtracted out. Regions of necrosis or dead tumor cells were also excluded. All pathology data procedures aforementioned were confirmed with an animal pathologist.

F. Statistical Analysis

Statistical analysis was done for determining differences between groups with a Student's t-test performed in MATLAB with a two-tailed analysis and $\alpha = 0.05$. Linear regression and

exponential fit of data was done in Excel for data sets with these apparent trends.

III. RESULTS

A. EVE System Detects Tumor Stiffness Heterogeneity and Differentiates Between Tumor, Spleen, and Pancreas Tissue

Fig. 3 shows that EVE can detect stiffness heterogeneity as well as distinguish non-tumor tissue and necrotic regions. It is clearly visible from the MT histology image that pancreas tissue (top left) is stained in dark purple, necrotic regions (bottom right) in light pink and viable tumor tissue in darker pink. While it is virtually impossible to identify tumor from pancreas tissue in the white light images, Young's modulus (YM) maps obtained from EVE can distinguish this difference. Both pancreas and necrotic regions were much softer than tumor tissue. Fig. 3B illustrates the average YM detected from spleen and pancreas tissue, found in 8 samples to be 4.0 ± 0.3 kPa and 2.3 ± 0.3 kPa, respectively. This data set provided validation results for EVE's feasibility to produce correct stiffness maps as these values agree with previously reported YM of murine organs. Yu *et al.* (2018) showed spleen's YM of rats to be 3.9 ± 0.6 kPa while Rice *et al.* (2017) reported mouse pancreas stiffness ranging from 1 to 4 kPa as PDAC progressed in genetically engineered mouse models [21], [22]. Even though these tissues are excluded from tumor analysis in this study, the measurements help to confirm the feasibility of using EVE in tumor stiffness mapping.

B. EVE System Has the Resolution Necessary to Study Extracellular Matrix (ECM) Heterogeneity in PDAC Tumors as Compared to Ultrasound Elastography

A comparison between UE and EVE is carried out with the result displayed in Fig. 4. Ultrasound B mode and elastography map were constructed using an established technique [14]. After that, EVE was used to measure tumor stiffness and a side-by-side comparison is illustrated in Fig. 4A. Generally, both UE and EVE agree on the level of stiffness heterogeneity in the tumor as well as the location of high stiffness. However, EVE, with the ability to resolve better spatial resolution, reveals a more refined stiffness map that displays similar patterns to the collagen profile in Fig. 4B. Expanded regions in Fig. 4C again show that stiffness information at a sufficient spatial resolution can reflect the collagen distribution within tumors.

C. Collagen Content in PDAC Tumors is Correlated With Reported Young's Modulus Values, Both of Which Display Extreme Heterogeneity

Tumor analysis, both globally and regionally, shows a strong correlation between stiffness and tumor collagen. Fig. 5A visually represents the high heterogeneity observed in both stiffness

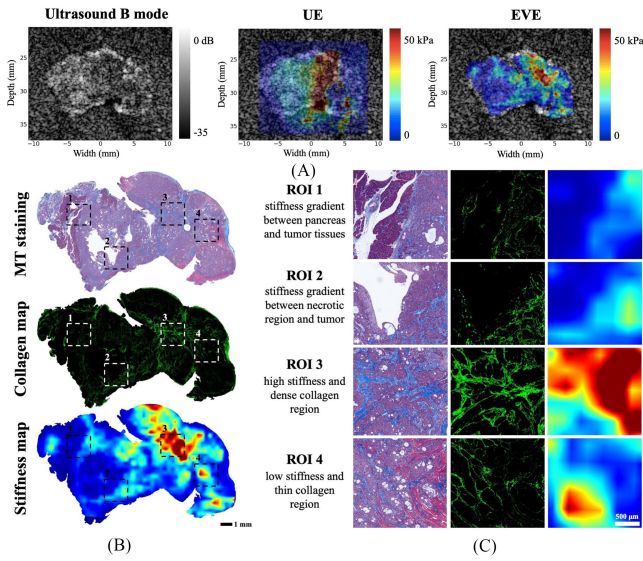


Fig. 4. Comparison between UE and EVE stiffness map. (A) Elastography imaging data from both systems are displayed to highlight similar pattern of stiffness heterogeneity. (B) Stiffness map obtained from EVE system with better spatial resolution allows for direct comparison between stiffness and collagen pattern in the tumor. (C) Expanded images of different ROIs highlight the correlation between stiffness and collagen percentage in PDAC tumors.

and collagen maps for AsPC-1 and BxPC-3 tumors. The overlay of stiffness and collagen information illustrates the agreement of higher stiffness regions with denser collagen regions. **Fig. 5B** reports the global average collagen content of AsPC-1 ($n = 13$) and BxPC-3 ($n = 14$) tumors to be 9.6 ± 2.7 percent and 13 ± 3 percent, respectively. Average AsPC-1 tumor stiffness is also lower than BxPC-3 values, 32 ± 11 kPa and 46 ± 24 kPa. Both of these measurements are statistically significant. Regional analysis to investigate both lower stiffness and higher stiffness regions in each tumor shows a linear relationship between Young's modulus values and collagen percentage in tumors, as showed in **Fig. 5C** with $R^2 = 0.59$. Regional analysis also suggests that collagen content in the tumors could reach up to 25% and tumor stiffness in between 5 and 150 kPa.

D. The Inverse Relationship Between Stiffness and Drug Distribution in PDAC Tumors Suggests the Potential of Elastography as a Surrogate for Tumor Drug Uptake

Whole tumor drug distribution and Young's modulus map are displayed in **Fig. 6A** to demonstrate the potential of stiffness as a surrogate for drug uptake globally in PDAC tumors. **Fig. 6B** provides regional information to highlight the inverse relationship between drug uptake and tumor stiffness. Less drug is accumulated in ROI 1 which is stiffer and contains more collagen while more uptake is observed in ROI 2 which is softer and has less collagen. In addition, more vessels are recorded in ROI 2 as compared to ROI 1. In **Fig. 6(C)–(D)**, the inverse relationship of stiffness to both drug uptake and patent vessels is highlighted in both tumor lines. Young's modulus

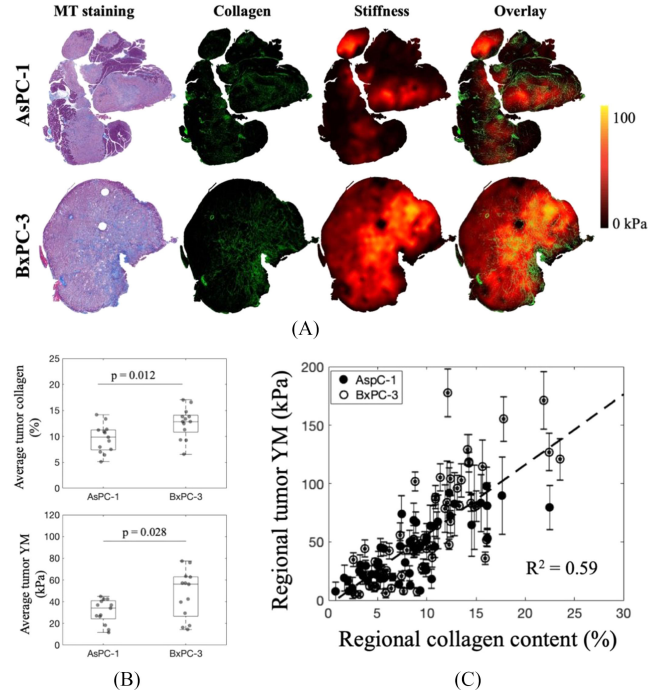


Fig. 5. Stiffness and collagen content in PDAC tumors are highly correlated both globally and regionally. (A) Visualization of stiffness, collagen and the overlay between two parameters show a good correlation in both AsPC-1 and BxPC-3 tumor lines. (B) AsPC-1 tumors contain 9.6 ± 2.7 percent collagen and average stiffness of 32 ± 11 kPa. As for BxPC-3, collagen percentage is averaged at 13 ± 3 percent and stiffness measured at 46 ± 24 kPa. Both of these quantities are statistically significant between AsPC-1 and BxPC-3 tumors. (C) Regional analysis to examine high stiffness and low stiffness regions demonstrates a linear correlation between Young's modulus and collagen profile with $R^2 = 0.59$. For each tumor, two high-stiffness and two low-stiffness regions were chosen (AsPC-1: $n = 13$, ROIs = 52; BxPC-3: $n = 14$, ROIs = 56).

and BPD fluorescence intensity data is a linear fit for both AsPC-1 and BxPC-3 with $R^2 = 0.66$ and $R^2 = 0.59$. More drug is accumulated in AsPC-1 tumors based on the average fluorescence intensity in **Fig. 6C**. Patent vessel density drastically reduces as stiffness increases for both tumor lines as illustrated in **Fig. 6D**.

IV. DISCUSSION

This study demonstrates that ex vivo stiffness mapping at 300-micron resolution could accurately represent the entire tumor-wide stiffness heterogeneity in both AsPC-1 and BxPC-3 xenograft models. The range of variation in stiffness values is visualized by EVE for the first time, to match the same level of variation of collagen network within a tumor (**Fig. 4(B)–(C)**). In our previous work, Nieskoski *et al.* (2017) generated a prediction of total tissue pressure maps with profound heterogeneity due to the strong correlation between point-probed solid stress measurements and surrounding collagen area fraction in PDAC tumors [16]. This work has confirmed that tumor stiffness is also strongly correlated with stroma variation. Understanding PDAC tumor physical and biological connection is crucial because the

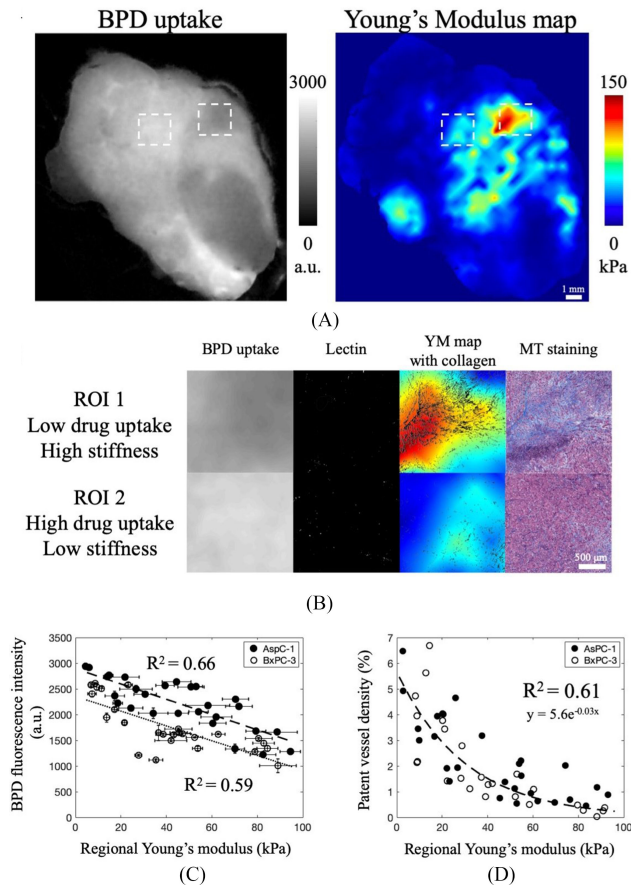


Fig. 6. PDAC tumor stiffness is inversely correlated with drug uptake and patent vessel data. (A) Whole-tumor visualization of BPD fluorescence distribution and stiffness heterogeneity obtained from EVE. (B) Close-up regions of low and high drug uptake reveal the inverse relationship with stiffness and collagen distribution. (C) Tumor YM is inversely correlated to BPD distribution in AsPC-1 and BxPC-3, with higher uptake in AsPC-1 tumors. (D) Tumor YM limits patent vessels which explains the limited drug penetration. For each tumor, two high-stiffness and two low-stiffness regions were chosen. There were 3 ROIs omitted since the vessel density percentage was essentially zero, and those ROIs had stiffness values greater than 100 kPa. (AsPC-1: $n = 7$, ROIs = 27; BxPC-3: $n = 7$, ROIs = 26).

practicality of stiffness imaging surpasses other tissue biomechanics quantities due to its non-invasive potential. Meanwhile, this finding emphasizes the need for resolution improvement of wide-field elastography systems such as UE and MRE to be at least on the resolution scale of 100's of microns to truly reflect biological variations in the tumor microenvironment. Furthermore, if imaging of stiffness is not achieved on this small spatial resolution scales, it is conceivable that highly inaccurate stiffness values may be obtained by partial volume averaging of the true values.

When analyzed region by region, the linear relationship between stiffness and collagen content (Fig. 5C) not only corroborates similar findings measured by UE [14], but also resonates with clinical data from Harada *et al.* (2017) in which a patient's pancreatic stiffness was correlated with fibrosis percentage ($R^2 = 0.58$) [23]. Another clinical study [24], in which advanced pancreatic cancer patients were treated with nab-paclitaxel to

target tumor stroma, came to the conclusion that elastography should be further investigated as data suggested the link between tumor stiffness and stroma modification. The study pointed out that even though the number of activated cancer-associated fibroblasts (CAF) did not change for treated and untreated cohorts, overall tumor stiffness measured by UE decreased for those with treatment responses. This finding is in agreement with the results presented by Laklai *et al.* (2010) that tumor stiffening could be a better indicator of stroma modification than bulk collagen abundance or total collagen proteins, especially when dense fibrosis is a product of both physical and genetic changes [10]. These findings underscore the potential use of elastography in explaining controversial results [25], [26] of anti-stromal therapies.

Despite the complexity and ongoing controversy underlying PDAC ECM remodeling, it is important to recognize that tumor stiffening is a universal physical phenotype to reflect PDAC transformation, with high potential for prognostic imaging or use in assessment of response or lack of response. However, appreciation of the value of the heterogeneity and spatial resolution can only motivate the need for further understanding of how this affects therapeutic delivery and response. Data from Fig. 6 showcases the possibility of exploiting stiffness information as a surrogate for drug penetration. Fig. 6A illustrates drug distribution and stiffness map from a global view whereas Fig. 6B displays two samples in which stiffer, collagen-denser region results in lower drug uptake and limited patent vessel area. Fig. 6C demonstrates the linear relationship between drug uptake and stiffness measurements in both AsPC-1 and BxPC-3. AsPC-1 tumors have higher BPD fluorescence intensity which aligns with information showed in Fig. 5B that on average AsPC-1 tumors are softer. The exponential fit between patent vessel area and regional stiffness corroborates the idea that growth-induced solid stress compresses blood vessels and CAF-depleted tumors had larger vessel diameters [27]. Considering it is widely accepted that functional blood vessels play a vital role in solid tumor interstitial transport, elastography imaging with an attempt to study the effect of tumor biology on drug transport should achieve a spatial resolution matching the capillary spacing, or hundreds of microns. Only then, tumor mechanics information will truly reflect biological changes with respect to transport efficiency.

This study has three main limitations. With pancreatic xenograft models implanting AsPC-1 and BxPC-3, the immunodeficient mice may not fully recapitulate the immune response promised by genetically-engineered mouse models [28]. For the purpose of demonstrating the potential of high-resolution elastography information in studying PDAC tumor microenvironment, current orthotopic xenograft models have proven to be adequate. It is necessary to acknowledge the mismatch between fresh and fixed tissue geometries, which compromises the accuracy of the image co-registration process. Inserting metal pins significantly facilitate this process of providing fiducial markers, to allow alignment and reasonable spatial match for this study. Furthermore, improved image co-registration process could allow for analysis of whole-tumor with ideal spatial resolution of hundreds of microns. Another limitation comes from

the edge effect of slicing the tumor embedded in gel and tissue stress relaxation, both of which result in tissue deformation. The stiffness values obtained from the tumor boundary would take into account the soft gel beneath therefore reported YM would be lower than actual values at these locations. However, tumor stiffness heterogeneity across the tumor area is an apparent observation despite peritumoral errors.

V. CONCLUSION

This study has demonstrated that with higher quality of elastographic imaging, stiffness information and its heterogeneity provide more spatial detail into how tumor mechanics could reflect changes in tumor biology and phenotypes. However, the fact that the spatial resolution required to allow biologically meaningful and accurate imaging is higher than what can be achieved with any diagnostic method suggests that further improvements in imaging tools must be developed before this can become a routine tool. The images in this work provide the core rationale for developing diagnostic imaging systems that might capture this level of spatial information in a non-invasive manner. Additionally, this existing system can be used as an ex vivo assay of response to anti-stromal therapies or acute invasive treatments such as irreversible electroporation [29] or photodynamic therapy [30].

ACKNOWLEDGMENT

The authors acknowledge the NCCC light microscopy shared resource (IPIM) supported in part by NCI Cancer Center Support Grant 5P30 CA023108-37.

REFERENCES

- [1] V. P. Chauhan *et al.*, "Delivery of molecular and nanoscale medicine to tumors: Transport barriers and strategies," *Annu. Rev. Chem. Biomol. Eng.*, vol. 2, no. 1, pp. 281–298, Jul. 2011.
- [2] M. E. Valsecchi *et al.*, "Recent treatment advances and novel therapies in pancreas cancer: A review," *J. Gastrointest. Cancer*, vol. 45, no. 2, pp. 190–201, Jun. 2014.
- [3] A. Adamska, A. Domenichini, and M. Falasca, "Pancreatic ductal adenocarcinoma: Current and evolving therapies," *Int. J. Mol. Sci.*, vol. 18, no. 7, Jun. 2017.
- [4] B. H. O'Neil *et al.*, "A phase II/III randomized study to compare the efficacy and safety of rigosertib plus gemcitabine versus gemcitabine alone in patients with previously untreated metastatic pancreatic cancer," *Ann. Oncol. Off. J. Eur. Soc. Med. Oncol.*, vol. 26, no. 9, pp. 1923–9, 2015.
- [5] G. Fountzilas *et al.*, "Gemcitabine combined with Gefitinib in patients with inoperable or metastatic pancreatic cancer: A phase II study of the hellenic cooperative oncology group with biomarker evaluation," *Cancer Invest.*, vol. 26, no. 8, pp. 784–793, Jan. 2008.
- [6] A. De Jesus-Acosta *et al.*, "A phase II study of the gamma secretase inhibitor RO4929097 in patients with previously treated metastatic pancreatic adenocarcinoma," *Invest. New Drugs*, vol. 32, no. 4, pp. 739–745, Aug. 2014.
- [7] R. K. Jain, J. D. Martin, and T. Stylianopoulos, "The role of mechanical forces in tumor growth and therapy," *Annu. Rev. Biomed. Eng.*, vol. 16, pp. 321–46, Jul. 2014.
- [8] T. P. Padera *et al.*, "Pathology: Cancer cells compress intratumour vessels," *Nature*, vol. 427, no. 6976, p. 695, Feb. 2004.
- [9] V. P. Chauhan *et al.*, "Angiotensin inhibition enhances drug delivery and potentiates chemotherapy by decompressing tumour blood vessels," *Nat. Commun.*, vol. 4, no. 1, p. 2516, Dec. 2013.
- [10] H. Laklai *et al.*, "Genotype tunes pancreatic ductal adenocarcinoma tissue tension to induce matricellular fibrosis and tumor progression," *Nat. Med.*, vol. 22, no. 5, pp. 497–505, 2016.
- [11] N. Harada *et al.*, "Preoperative pancreatic stiffness by real-time tissue elastography to predict pancreatic fistula after Pancreaticoduodenectomy," *Anticancer Res.*, vol. 37, no. 4, pp. 1909–1915, Apr. 2017.
- [12] Q. Fang *et al.*, "Ultrahigh-resolution optical coherence elastography through a micro-endoscope: Towards in vivo imaging of cellular-scale mechanics," *Biomed. Opt. Express*, vol. 8, no. 11, pp. 5127–5138, Nov. 2017.
- [13] H. Wang *et al.*, "Elastographic assessment of xenograft pancreatic tumors," *Ultrasound Med. Biol.*, vol. 43, no. 12, pp. 2891–2903, Dec. 2017.
- [14] H. Wang *et al.*, "Elastography can map the local inverse relationship between shear modulus and drug delivery within the pancreatic ductal adenocarcinoma microenvironment," *Clin. Cancer Res.*, p. clincanres.2684.2018, Oct. 2018.
- [15] S. Wang and K. V. Larin, "Optical coherence elastography for tissue characterization: A review," *J. Biophotonics*, vol. 8, no. 4, pp. 279–302, Apr. 2015.
- [16] M. D. Nieskoski *et al.*, "Collagen complexity spatially defines microregions of total tissue pressure in pancreatic cancer," *Sci. Rep.*, vol. 7, no. 1, p. 10093, Dec. 2017.
- [17] A. D. C. Leonardi *et al.*, "Intracranial pressure increases during exposure to a shock wave," *J. Neurotrauma*, vol. 28, no. 1, pp. 85–94, Jan. 2011.
- [18] E. Pinet, A. Pham, and S. Rioux, "Miniature fiber optic pressure sensor for medical applications: An opportunity for intra-aortic balloon pumping (IABP) therapy," in *Proc. SPIE, 17th Int. Conf. Opt. Fiber Sensors*, vol. 5855, 2005, pp. 234–237.
- [19] A. Kolipaka *et al.*, "Magnetic resonance elastography as a method for the assessment of effective myocardial stiffness throughout the cardiac cycle," *Magn. Reson. Med.*, vol. 64, no. 3, pp. 862–870, Sep. 2010.
- [20] A. M. Laughney *et al.*, "Scatter spectroscopic imaging distinguishes between breast pathologies in tissues relevant to surgical margin assessment," *Clin. Cancer Res.*, vol. 18, no. 22, pp. 6315–25, Nov. 2012.
- [21] X. Yu *et al.*, "Needle-shaped ultrathin piezoelectric microsystem for guided tissue targeting via mechanical sensing," *Nat. Biomed. Eng.*, vol. 2, no. 3, pp. 165–172, Mar. 2018.
- [22] A. J. Rice *et al.*, "Matrix stiffness induces epithelial–mesenchymal transition and promotes chemoresistance in pancreatic cancer cells," *Oncogenesis*, vol. 6, no. 7, pp. e352–e352, Jul. 2017.
- [23] N. Harada *et al.*, *Anticancer Research*, Potamitis Press, 1981.
- [24] R. Alvarez *et al.*, "Stromal disrupting effects of nab-paclitaxel in pancreatic cancer," *Br. J. Cancer*, vol. 109, no. 4, pp. 926–33, Aug. 2013.
- [25] A. D. Rhim *et al.*, "Stromal elements act to restrain, rather than support, pancreatic ductal adenocarcinoma," *Cancer Cell*, vol. 25, no. 6, pp. 735–747, Jun. 2014.
- [26] B. C. Özdemir *et al.*, "Depletion of carcinoma-associated fibroblasts and fibrosis induces immunosuppression and accelerates pancreas cancer with reduced survival," *Cancer Cell*, vol. 25, no. 6, pp. 719–34, Jun. 2014.
- [27] T. Stylianopoulos *et al.*, "Causes, consequences, and remedies for growth-induced solid stress in murine and human tumors," *Proc. Natl. Acad. Sci. U. S. A.*, vol. 109, no. 38, pp. 15101–8, Sep. 2012.
- [28] B. D. Krempsey and K. H. Yu, "Preclinical models of pancreatic ductal adenocarcinoma," *Chin. Clin. Oncol.*, vol. 6, no. 3, pp. 25–25, Jun. 2017.
- [29] R. C. G. Martin *et al.*, "Irreversible electroporation therapy in the management of locally advanced pancreatic adenocarcinoma," *J. Am. Coll. Surg.*, vol. 215, no. 3, pp. 361–369, Sep. 2012.
- [30] M. T. Huggett *et al.*, "Phase I/II study of verteporfin photodynamic therapy in locally advanced pancreatic cancer," *Br. J. Cancer*, vol. 110, no. 7, pp. 1698–1704, Apr. 2014.